Close-Space Sublimation – Versatile Deposition Process for Efficient Perovskite/Silicon Tandem Solar Cells

Alexander Diercks[a,b†], Sofía Chozas-Barrientos[c†], Lidón Gil-Escrig[c], Federico Ventosinos[c,d], Inma Gomar-Fernández[c], Cristina Roldán-Carmona[c], Tonghan Zhao[a,b], Julian Petermann[a,b], Perrine Carroy[e], Delfina Muñoz[e], Paul Fassl[a,b], Michele Sessolo[c], Ulrich W. Paetzold[a,b,†*] and Henk J. Bolink[c,†*]

[a] *Light Technology Institute, Karlsruhe Institute of Technology, Engesserstrasse 13, 76131 Karlsruhe, Germany*

[b] *Institute of Microstructure Technology, Karlsruhe Institute of Technology, Hermann-von-Helmholtz-Platz 1, 76344 Eggenstein-Leopoldshafen, Germany*

[c] *Instituto de Ciencia Molecular, Universidad de Valencia, C/Catedrático J. Beltrán 2, 46980 Paterna, Spain*

[d] *Instituto de Física del Litoral (IFIS-Litoral), CONICET-UNL, Güemes 3450, S3000GLN, Santa Fe, Argentina*

[e] *Université Grenoble Alpes, CEA, LITEN, Campus INES, 50 avenue du Lac Léman, F-73375 Le Bourget-du-Lac, France*

[†] *equal contribution*

[*] *corresponding authors*

contact: ulrich.paetzold@kit.edu; henk.bolink@uv.es

Keywords: close-space sublimation, perovskite solar cells, perovskite/silicon tandem solar cells, thermal evaporation

Abstract

The envisaged breakthrough of perovskite photovoltaic technologies demands rapid advances in scalable fabrication methods. In this study, we present close-space sublimation (CSS) as a vacuum-based, industrially relevant deposition method for the fabrication of high-quality wide-bandgap perovskite absorbers (1.63 eV), achieving PCEs of up to 18.5% in *p-i-n* single-junction devices. Monolithic integration of the perovskite top-cells onto planar, nano-, and micro-textured silicon bottom cells, revealed consistent optoelectronic and morphological properties across all configurations, without requiring adjustments of deposition parameters. This robustness is confirmed through comprehensive characterization techniques, including external quantum efficiency, Suns-V_{OC} with selective illumination, scanning electron microscopy, and grazing-incidence wide-angle X-ray scattering. The resulting tandem devices reached PCEs of up to 24.3%, with minimal variation across the different bottom cells. Our findings highlight the broad process window and versatility of CSS, positioning it as a promising deposition method for rapid and industry-suitable fabrication of efficient monolithic perovskite/silicon tandem solar cells.

Main

Bridging the gap between laboratory- and industrial-scale fabrication remains a key challenge for advancing industrialization of perovskite photovoltaics.[1–5] In this regard, advances on industrially relevant deposition methods for rapid processing and efficient upscaling are pivotal.[1,6–8] This urge has been further amplified by recent reports of power conversion

efficiencies (PCEs) exceeding 34% in perovskite/silicon tandem solar cells, already surpassing those of market-leading silicon technologies.[9] Despite being severely underrepresented in literature, vapor phase deposition offers key benefits when it comes to scalable processing: i.e. homogeneous large-area coating and continuous in-line processing.[2,10–13] Furthermore, vapor phase deposition allows for conformal coverage of textured surfaces, essential for the monolithic integration of perovskite absorbers into two-terminal (2T) tandem solar cells (TSCs) with textured silicon bottom cells.[6,14,15] To date, most studies exploring vapor phase deposition for the fabrication of perovskite solar cells (PSCs) have focused on either co-deposition or sequential layer deposition from point sources in high vacuum. Reported power conversion efficiencies (PCEs) using these approaches have reached up to 21% and 26.4% in single-junction (SJ) PSC configurations, respectively.[16,17] The highest reported PCE for a fully textured 2T perovskite/silicon TSC fabricated *via* vapor phase deposition is 24.5% using a co-deposited $MA_{0.5}FA_{0.63}PbI_{3.13}$ perovskite top cell as demonstrated by Roß *et al*.[15] While these results highlight the potential of vapor phase deposition processes for the fabrication of high efficiency perovskite-based solar cells, their slow deposition rates compared to solution-based methods remain a significant hurdle to efficient industrialization.[4,18,19]

Close-space sublimation (CSS) has recently emerged as a new deposition technique for perovskite photovoltaics that bears the potential to reach high deposition rates for the organic precursor components, while maintaining both high performance and the key advantages of vapor phase deposition.[20,21] In CSS, the gap between the substrate with the inorganic scaffold and the organic precursor source is drastically reduced compared to established thermal evaporation setups. Thereby, for gaps of a few millimeters or less, the organic precursors can be deposited at much higher rates and elevated working pressures, typically in the range of 1-100 mbar.[20,21] Moreover, material usage is much more efficient compared to sublimation from point sources. CSS processes employ elevated substrate temperatures during the deposition, resulting in an in-situ conversion of the inorganic scaffold to the perovskite phase.[21] First reports on a CSS-based fabrication process for $MAPbI_3$ PSCs were published in 2015 by Li *et al.* achieving PCEs of up to 16.2%.[22] Guesnay *et al.* reported the first wide-bandgap (WBG) PSC, reaching maximum PCEs of 16.8% for a bandgap of 1.63 eV.[23] Further studies on similar fabrication processes, mainly close-space vapor transport, show PCEs of up to 22.45% for narrow bandgap perovskite compositions[24–26]. Critically, all of these studies implement solution-processed single-use organic sources, unsuitable for continuous in-line vacuum-based processing.[23–28] More recently, Rodkey *et al.* demonstrated a fully solvent-free CSS setup employing a reusable organic source design, operational for more than 28 depositions, reaching maximum PCEs of 18.7% for $FACsPbI_3$:Cl PSCs.[21] Despite recent progress, there remains a notable lack of research on WBG perovskites suitable for tandem photovoltaics that are fabricated using industrially compatible CSS processes.

In response, this work showcases the first demonstration of CSS using a solvent-free organic source as an effective technique to fabricate fully vacuum-processed, high quality WBG perovskite absorbers at high deposition rates. These absorbers enable SJ PSCs with PCEs of up to 18.5%, as well as planar and fully textured 2T perovskite/silicon TSCs, achieving PCEs of 23.5% and 24.5% respectively. To evaluate the perovskite thin film properties, scanning electron microscopy (SEM), X-ray diffraction (XRD) and photoluminescence (PL) measurements are employed. Combined with current-voltage (*J-V)* analysis and external quantum efficiency (EQE) measurements, we reveal the excellent optoelectronic properties of the fabricated SJ PSCs. Further analysis of the perovskite absorber layer deposited on planar, nanometer- and micrometer-size textured silicon heterojunction bottom cells using SEM and grazing-incidence wide-angle X-ray scattering (GIWAXS) provides insight into growth mechanisms on differently textured substrates. The successful integration of these films into

2T perovskite/silicon TSCs is confirmed by in-depth sub-cell characterization using EQE and Suns-V_{OC} with selective illumination, revealing consistent perovskite layer qualities across all bottom cell morphologies. Our results demonstrate the high versatility of CSS for the fabrication of efficient SJ PSCs and 2T perovskite/silicon TSCs on textured silicon bottom cells, proving its potential as an industrial-scale high-throughput fabrication process.

Efficient Wide-Bandgap Perovskite Solar Cells

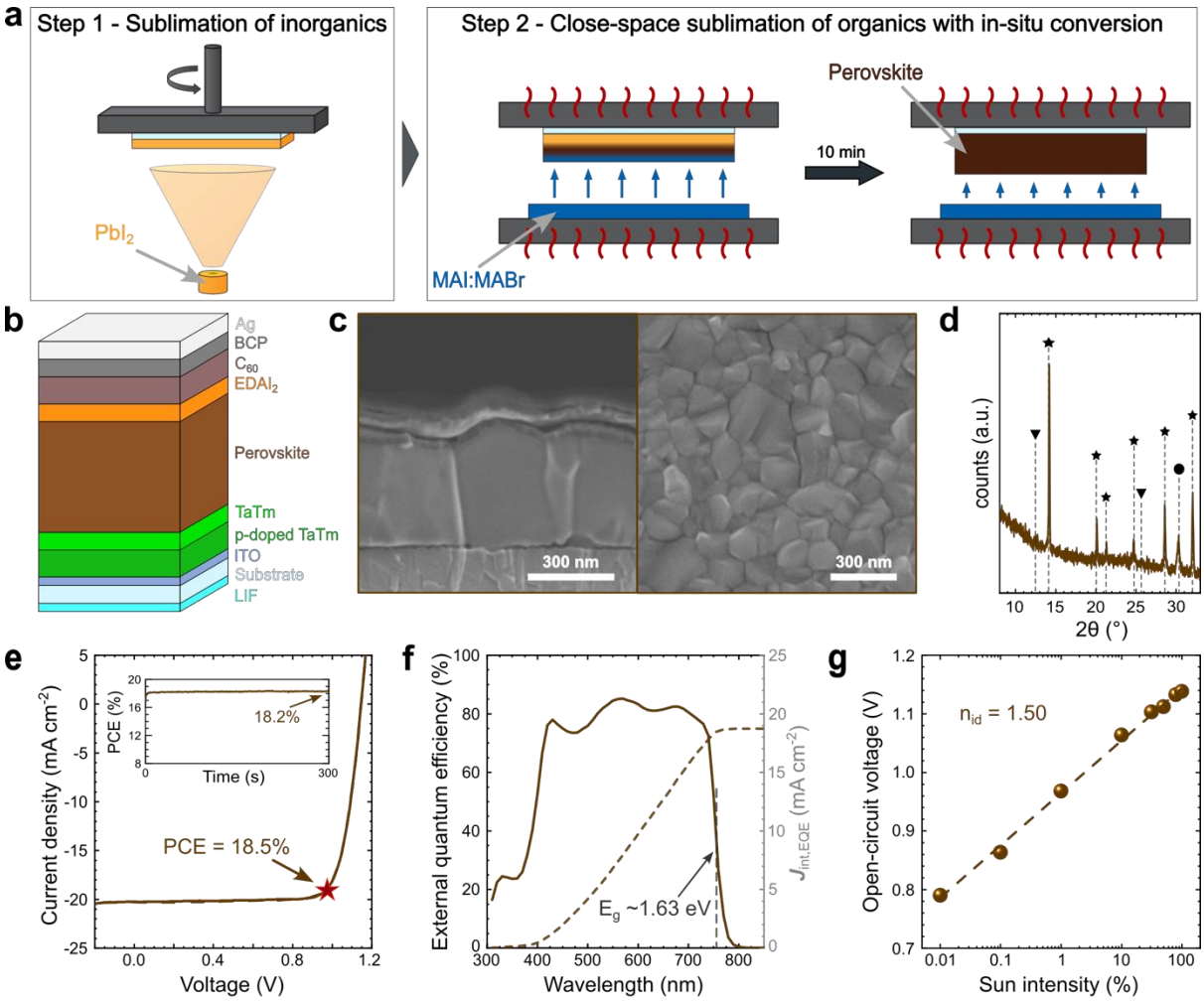

Figure 1: a Schematic of the 2-step processed perovskite absorber layer using physical vapor deposition from a point source for the inorganic precursor (PbI_2) materials and close-space sublimation for the organic precursor materials (MAI, MABr) with in-situ conversion to the perovskite phase. **b** Fully vacuum-processed layer stack of fabricated perovskite solar cells (PSCs) in *p-i-n* architecture with $EDAI_2$ and LiF as surface passivation and anti-reflective coating respectively. **c** Scanning electron microscopy (SEM) images of cross-section of PSC (left) and corresponding surface of perovskite absorber layer (right). **d** X-ray diffraction (XRD) pattern of PSC. Triangles, stars, and circles represent PbI_2 perovskite and ITO diffraction peaks, respectively. **e** Current-voltage (*J-V*) characteristic of champion PSC with maximum power point (MPP)-tracking for 300 seconds. **f** Corresponding external quantum efficiency (EQE) measurement with integrated current density and highlighted bandgap **g** Light-intensity dependent V_{OC} measurements, taken from corresponding *J-V* measurements, with extracted ideality factor (n_{id}).

In this work, a sequential vapor phase deposition process is pioneered to fabricate MA-based WBG perovskite absorber layers for application in 2T perovskite/silicon TSCs. A schematic of the fabrication process is shown in **Fig. 1a**. The first step comprises the thermal sublimation

of the PbI_2 inorganic precursor leading to a 250 nm thick inorganic scaffold layer. The second step involves the close space sublimation of the organic cations, namely a mixture of methylammonium iodide (MAI) and methylammonium bromide (MABr) with a relative mass ratio of 3 mg_{MAI} : 1 mg_{MABr}. Given a substrate temperature of 120 °C during the CSS step, the sublimed MAI:MABr reacts in-situ with the PbI_2 scaffold and starts forming the polycrystalline perovskite thin film.[21] The close gap between the substrate and the MAI:MABr source allows the CSS deposition to be easily controlled by the pressure in the vacuum chamber. The MAI:MABr source, which is maintained at 100 °C, begins subliming as soon as the pressure within the chamber is reduced. When the target pressure of 1 mbar is reached, the system is kept at this pressure for 10 minutes, sufficient to fully convert the PbI_2 scaffold into the final methylammonium lead iodide/bromide ($MAPb(I_{0.79}Br_{0.21})_3$) perovskite film (**Fig. S1**). The deposition is terminated by venting the chamber with N_2 and bringing the chamber back to atmospheric pressure. An additional annealing step after the CSS deposition of the organic precursors is found to be of importance to further improve the performance of the final PSCs. While as-deposited PSCs already exhibit respectable performance with median PCEs of 14.4% (**Fig. S2**, **Fig S3**, **Table 1**), additional annealing of 10 min at 100 °C in a humidity-controlled environment (relative humidity ~35%) boosts the PCEs up to more than 16% (**Fig. S2**, **Table 1**).

The champion device, with an optimized fully vacuum-processed layer stack (LiF/ITO/p-doped TaTm/TaTm/$MAPb(I_{0.79}Br_{0.21})_3$/$EDAI_2$/$C_{60}$/BCP/Ag) (**Fig. 1b**), achieves a maximum PCE of 18.5%, with negligible hysteresis and a stabilized power output of 18.2% under maximum power point (MPP)-tracking (**Fig. 1e**)**.** The 50 mV increase in open-circuit voltage (V_{OC}) and 0.7 mA cm^{-2} enhancement in short-circuit current density (J_{SC}) compared to the annealed device are attributed to the use of $EDAI_2$ for surface passivation and LiF as an anti-reflective coating (**Fig. S4**, **Table 1**). With a bandgap of 1.63 eV, as extracted from corresponding EQE measurements (**Fig. 1f**), this performance represents the highest reported PCE for fully vacuum-processed wide-bandgap (E_g > 1.6 eV) PSCs in the *p-i-n* architecture using a pure MA-based composition.[29] SEM imaging reveals large grains with a compact structure throughout the absorber layer (**Fig. 1c**), while XRD analysis confirms the quantitative formation of the perovskite with no detectable residual PbI_2 (**Fig. 1d**). The additional annealing step further improves film morphology without altering its composition or crystallinity (**Fig. S1, Fig. S5, Fig. S6**). Light-intensity-dependent *J-V* measurements yield an ideality factor of n_{id} = 1.50 (**Fig. 1g, Table S1**), indicating low recombination losses.

Furthermore, to study the suitability of our CSS-processed WBG PSCs for tandem applications, semitransparent (ST) devices were fabricated. PCEs of the ST PSCs reach more than 16% under top illumination (**Table 1**, **Fig. S7**, **Fig S8**) showing great potential for the integration of CSS processed perovskite absorbers into tandem architectures.

Table 1: Photovoltaic parameters of the best-performing PSCs for the different architectures.

	PCE (%)	FF (%)	J_{SC} (mA cm^{-2})	V_{OC} (V)
as-deposited	14.6	70.2	19.6	1.06
annealed	16.2	74.5	19.7	1.10
with $EDAI_2$	17.4	79.9	19.1	1.14
with $EDAI_2$ & LiF	**18.5**	**79.2**	**20.3**	**1.15**
ST top-illuminated	16.2	75.3	19.5	1.10

Monolithic 2-terminal perovskite/silicon tandem solar cells

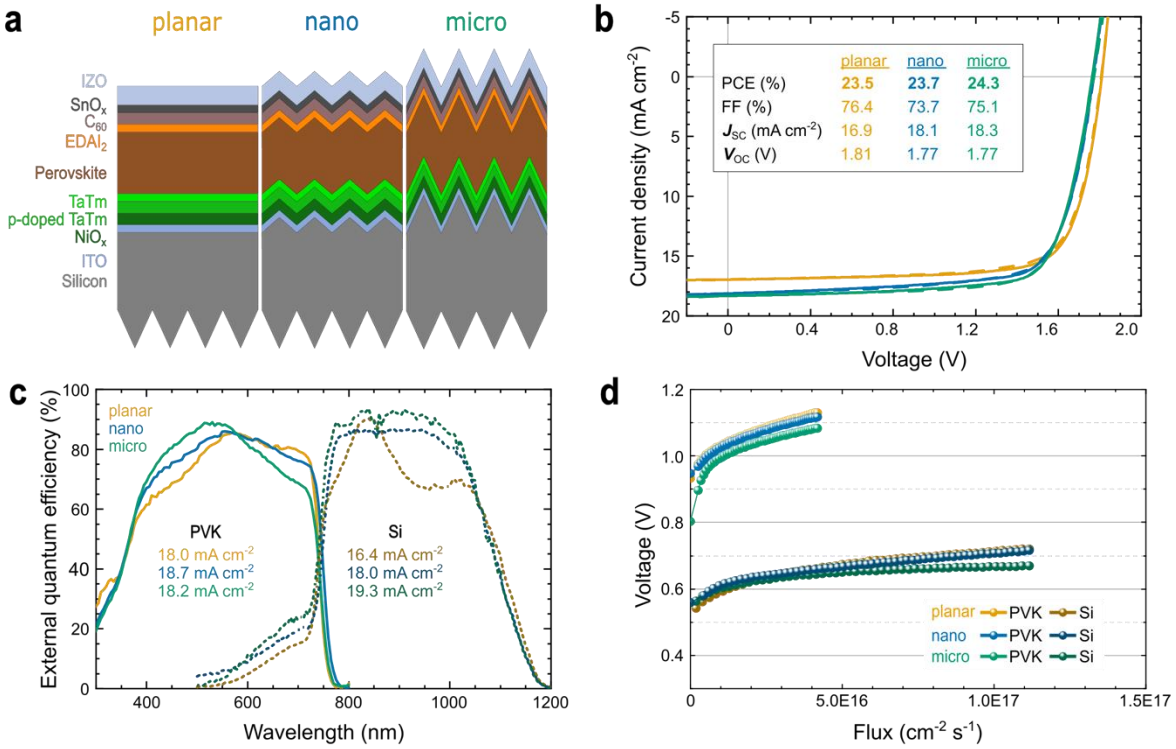

Figure 2: a Layer stacks of fabricated two-terminal perovskite/silicon tandem solar cells (TSCs) with differently textured silicon bottom cells (planar, nano-textured and micro-textured). **b** Current-Voltage (*J-V*) characteristics of champion TSCs for all three configurations with corresponding photovoltaic parameters. **c** External quantum efficiency (EQE) analysis of champion TSCs on planar, nano-textured and micro-textured silicon bottom cells. **d** Suns-V_{OC} with selective illumination measurements of both sub-cells of corresponding TSCs.

The CSS-processed WBG perovskite absorbers were successfully integrated into monolithic perovskite/silicon TSCs. To evaluate the versatility of the developed CSS process, silicon heterojunction bottom cells featuring three different morphologies were selected, namely planar, sub-micrometer pyramidal (nano-textured) and micrometer-scale pyramidal (micro-textured), representing both research-scale and industrially relevant architectures. The layer stack of the fabricated 2T TSCs (Si/ITO/NiO_x/p-doped TaTm/TaTm/MAPb($I_{0.79}Br_{0.21}$)$_3$/$EDAI_2$/C_{60}/SnO_x/IZO/Ag) was the same for all three configurations (**Fig. 2a**, **Fig. S9**). Notably, the perovskite deposition parameters were kept identical across all three bottom cell morphologies (PbI_2 layer thickness = 250 nm, T_{Source} = 100 °C, $T_{Substrate}$ = 120 °C and CSS deposition time = 10 minutes), while only the thicknesses of the charge transport layers and electrodes were adjusted to account for the increased surface area on the textured substrates. All configurations exhibit comparable performance, indicating a robust and solid process tolerance of CSS regardless of the substrate surface morphology (**Fig. 2b**). *J-V* measurements of the best-performing devices in each configuration reveal comparable $\boldsymbol{V_{OC}}$ ranging from 1.77-1.81 V and FF around 75%. The planar device achieves the highest V_{OC} (1.81 V), suggesting reduced interfacial recombination. In contrast, the nano- and micro-textured devices exhibit higher J_{SC}s of 18.1 mA cm^{-2} and 18.3 mA cm^{-2}, respectively, attributed to enhanced light trapping and increased optical path length enabled by surface texturing. Among all configurations, the micro-textured device achieves the highest PCE of 24.3%, outperforming the planar (23.5%)

and nano-textured (23.7%) configurations. This performance is among the highest reported PCEs for fully textured 2T perovskite/silicon TSCs employing vapor-phase-deposited perovskite absorbers.[15,30] These results highlight the robustness of the CSS process across different bottom cell morphologies and underscore its potential as a scalable, solvent-free deposition technique for high-throughput fabrication of efficient 2T TSCs on industrially relevant silicon substrates.

EQE analyses reveal a consistent integrated photocurrent density for the perovskite top cells across all three bottom cell morphologies, ranging from 18.0 mA cm^{-2} to 18.7 mA cm^{-2} (**Fig. 2c**), indicating uniform optical and electronic quality of the top absorber. As anticipated, the integrated photocurrent density of the silicon bottom cell exhibits a clear dependence on surface texturing, increasing from 16.4 mA cm^{-2} for the planar configuration to 18.0 mA cm^{-2} for nano-textured and 19.3 mA cm^{-2} for micro-textured surfaces. These findings are in excellent agreement with the trends observed in the *J-V* characteristics presented in **Fig. 2b**. Irrespective of the texture, all perovskite top cells exhibit identical bandgaps of ~1.66 eV as extracted from EQE, further demonstrating the robustness of the perovskite formation by our CSS process (**Fig. S10**). Compositional engineering of the perovskite absorber layer presents a promising strategy to optimize current matching tailored to the specific optical and electronic characteristics of each silicon bottom cell morphology. Suns-V_{OC} with selective illumination measurements reveal a consistent voltage generation of ~1.09 V for each perovskite top cell across all configurations, further underscoring the robustness of CSS (**Fig. 2d**). These measurements were conducted by selectively exciting the perovskite or silicon sub-cell using collimated LEDs at 450 nm and 940 nm, respectively. In combination with EQE analyses, the illumination intensities corresponding to one sun at the selected wavelengths (450 nm for the perovskite top cell and 940 nm for the silicon bottom cell) can be accurately determined, allowing for the extraction of the V_{OC} of each sub-cell (**Fig. S11**). Parasitic absorption and PL from blue excitation can generate a contribution from the silicon bottom cell to the voltage vs. flux measurement of the perovskite top cell, which can lead to an overestimation of the perovskite V_{OC}. To mitigate this, the V_{OC} of the perovskite top cell is estimated by subtracting the V_{OC} of the silicon bottom cell (**Fig. S11**) from the measured tandem device V_{OC} (**Fig. 2b**). Moreover, all three perovskite top cells exhibit a clear logarithmic dependence of voltage on light flux, indicating a low shunt leakage and efficient carrier extraction.[30] The observed uniformity in V_{OC}, together with the identical bandgaps of ~1.66 eV, further reinforces the reproducibility and reliability of the CSS process.

In-depth sub-cell characterization, combining EQE and Suns-V_{OC} analyses, demonstrates the capability of CSS to produce high-quality perovskite films on both planar and textured silicon substrates, confirming a wide and reliable process window for scalable tandem device fabrication.

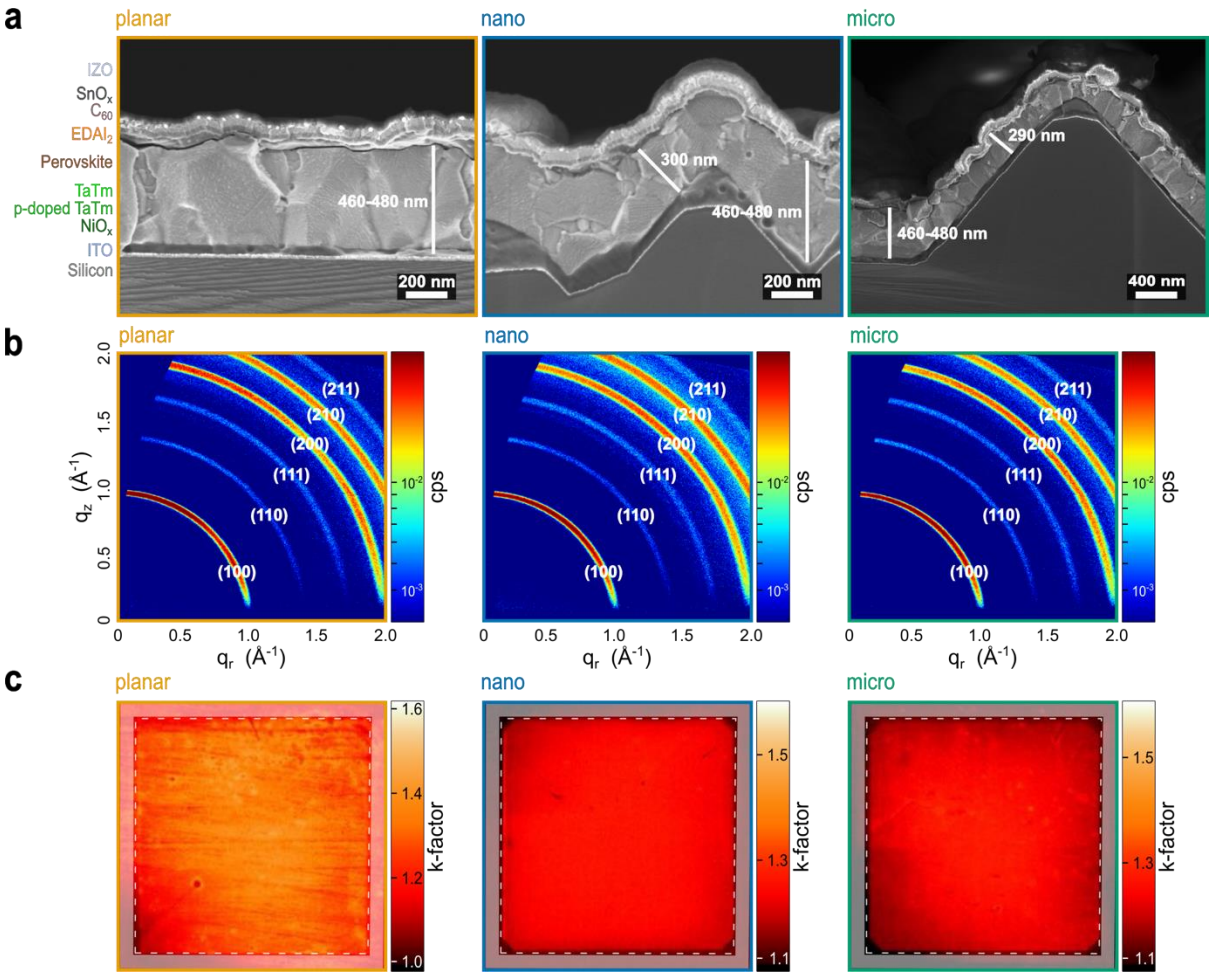

Figure 3: a Cross-sectional scanning electron microscopy (SEM) images of finished tandem solar cells (TSCs) on planar, nano- and micro-textured silicon bottom cells. **b** Grazing-incident wide-angle X-ray scattering (GIWAXS) measurements of corresponding TSCs. **c** Spatially resolved k-factor images derived from intensity-dependent photoluminescence (PL)-mapping of the active area (1 cm^2) of the perovskite thin films on planar, nano- and micro-textured silicon bottom cells.

Cross-sectional SEM imaging confirms a similar perovskite layer morphology across all three silicon bottom cell morphologies despite their different surface topographies (**Fig. 3a**). All configurations exhibit conformal coverage with similar horizontal grain sizes and pronounced columnar growth, comparable to the SJ reference. Furthermore, complete coverage all bottom cell morphologies by the perovskite absorber is observed, demonstrating the excellent deposition uniformity enabled by CSS (**Fig. S12**). Thickness measurements along the optical axis (light incident direction) reveal comparable perovskite film thicknesses of 460-480 nm across all configurations. However, when measured perpendicular to the pyramid facets, the effective perovskite film thickness on nano- and micro-textured substrates is reduced to approximately 300 nm due to the increased surface area, as expected. GIWAXS analyses (**Fig. 3b**) show similar patterns for all three configurations with no preferred growth orientation of the perovskite crystallites, as confirmed by the corresponding pole figures (**Fig. S13, Fig S14**). Additionally, all films exhibit similar degrees of crystallinity, with comparable full-width at half-maximum values for the (100)-perovskite peak, indicating a consistent microstructure across all silicon bottom cell morphologies. Spatially resolved k-imaging derived from intensity-dependent PL-mapping reveals comparable perovskite layer qualities and great homogeneity across the entire active area (1 cm^2) of the substrate in all three cases (**Fig. 3c**).[31,32] For both textured configurations (nano- and micro-textured) the perovskite layers exhibit similar k-factor values of ~1.2-1.3, while the perovskite layer in the planar configuration

shows slightly higher k-factors of ~1.3-1.4. These results further highlight the robustness of the CSS process, which enables uniform, conformal and high-quality perovskite film formation with consistent morphological, microstructural and opto-electronic properties independent of the texture of the underlying substrate and without the need to adjust deposition parameters. This distinguishes CSS from other deposition techniques such as co-sublimation, solution-based, or hybrid deposition methods, which typically require significant process modifications to accommodate varying surface morphologies.[14,33,34]

Our work pioneers CSS as a promising, industrially relevant deposition method for scalable, vacuum-based fabrication of efficient perovskite-based photovoltaics. We report the first demonstration of CSS for fully vacuum-processed wide-bandgap single-junction PSC in the *p-i-n* architecture, with PCEs up to 18.5% for a pure MA-based perovskite composition. These results underscore the potential of CSS to deliver competitive device performances for vapor-phase-deposited PSCs. The fast optimization cycling, enabled by the rapid CSS process compared to other typically much slower vapor-based deposition methods, will further accelerate the technological development of this technique. With exceptionally short deposition times of 10 minutes and champion PCEs of 24.3%, achieved for fully vacuum-processed 2T perovskite/silicon TSCs on industrially relevant silicon bottom cells, our work represents a promising start to an innovative deposition method with great potential for cost-effective and high-throughput processing.

Conclusion

Enhancing the deposition rate of vacuum-based processes remains a key challenge for the scalable fabrication of perovskite photovoltaics. In this work, we demonstrate a fully vacuum-based, solvent-free close-space sublimation (CSS) process for the rapid deposition of MA-based wide-bandgap perovskite solar cells (PSCs). A mixed organic MAI:MABr source is used to convert a sublimed PbI_2 inorganic scaffold into $MAPb(I_{0.79}Br_{0.21})_3$with a bandgap of 1.63 eV. With an optimized layer stack, power conversion efficiencies (PCEs) of up to 18.5% (stabilized at 18.2%) are achieved for opaque *p-i-n* single-junction devices. To date, this is the highest reported PCE for fully vacuum-processed PSCs in the *p-i-n* architecture using solvent-free CSS. We further demonstrate the successful integration of the developed wide-bandgap perovskite absorber into two-terminal (2T) perovskite/silicon tandem solar cells (TSCs) on silicon bottom cells with different surface morphologies (planar, nanometer-size and micrometer-size pyramids). Without adjusting the CSS deposition parameters to the different textured surfaces, the perovskite films show comparable optoelectronic properties, revealing a wide and robust process window. Furthermore, scanning electron microscopy and grazing-incidence wide-angle X-ray scattering analyses reveal similar morphologies and crystal growth of the perovskite layers on all three bottom cell morphologies. Sub-cell characterization *via* external quantum efficiency and Suns-V_{OC} with selective illumination measurements reveal consistent current generation and voltage output from the perovskite top cells, regardless of the underlying silicon bottom cell morphology. A champion PCE of 24.3% was achieved for fully micro-textured perovskite/silicon TSCs, comparable to the highest reported values for fully textured 2T TSCs with vapor-phase deposited perovskite absorbers. Our results highlight the versatility, scalability, and industrial relevance of CSS as a high-throughput, solvent-free deposition method for efficient two-terminal perovskite/silicon TSCs.

Methods

Materials

Pre-patterned ITO-coated glass substrates were purchased from Kintec Company. TaTm (N4,N4,N4'',N4''-tetra([1,1'-biphenyl]-4-yl)-[1,1':4',1''-terphenyl]-4,4''-diamine) was obtained from Tokyo Chemical Industry. CS90112 (2,2',2''-(cyclopropane-1,2,3-triylidene)tris(2-(p-cyanotetrafluorophenyl)acetonitrile)), PbI_2 (lead iodide), MAI (methylammonium iodide) and BCP (bathocuproine) were purchased from Luminescence Technology Corp. MABr (methylammonium bromide) was purchased from Greatcell Solar Materials. C_{60} (fullerene-C_{60}) was purchased from MBraun (Creaphys). $EDAI_2$ (ethylene-diammonium di-iodide) was purchased from Sigma-Aldrich Co.

Film and Device Fabrication

Single-Junction Perovskite Solar Cells

ITO-coated glass substrates were subsequently cleaned with soap (2% Mucasol™ in water), water and isopropanol in an ultrasonic bath, followed by 20 min UV-ozone treatment. The substrates were transferred to a vacuum chamber integrated in a nitrogen-filled glovebox and evacuated to a pressure of 10^{-6} mbar for the charge extraction layers' deposition. In general, the deposition rate for the TaTm and C_{60} was 0.5 $Å s^{-1}$ while the thinner BCP was deposited at 0.2 $Å s^{-1}$. For the p-doped HTL layer TaTm and CS90112 (as p-dopant) were co-sublimed at a rate of 0.8 and 0.12 $Å s^{-1}$ by heating them at temperatures of around 300 °C and 130 °C respectively. Ag was evaporated in a separate vacuum chamber using aluminum boats as sources. The PbI_2 inorganic scaffold was deposited at a rate of 1 $Å s^{-1}$ attained at a temperature of 250 °C. The rate and final thickness of 250 nm were controlled in an individual QCM placed above the PbI_2 source. For the organic precursor source for the CSS deposition step, MAI and MABr were mixed in the relative mass ratio of 3 mg_{MAI} : 1 mg_{MABr}. The mixture was then ground with a mortar to obtain a homogeneous mixture of fine powder. This powder was then evenly distributed in a metal tray, which serves as the source for the CSS process. After placing the samples above the source with a gap of 3 mm, both source and substrates were heated to the desired temperatures (T_{Source} = 100 °C and $T_{Substrate}$ = 120 °C). The chamber was then pumped down to 1 mbar and kept at this pressure for 10 min, sufficient to fully convert the inorganic scaffold to perovskite. After that, the chamber is vented with N_2 and brought back to atmospheric pressure. The additional annealing step (10 minutes at 100 °C) is carried out in a humidity-controlled setup with a relative humidity of ~35%. Afterwards, the samples were dynamically washed with 100 µl isopropanol for 20 seconds at 3000 rpm. $EDAI_2$ surface passivation layer was deposited in a high vacuum chamber at 10^{-6} mbar at a rate of about 0.1-0.15 $Å s^{-1}$.

Two-Terminal Perovskite/Silicon Tandem Solar Cells

Prior to tandem cell fabrication, silicon bottom cells were cleaned by sonicating for 5 min in acetone, then 5 minutes in IPA followed by a 15 min UV-ozone treatment. The additional NiO_x HTL layer (15 nm for planar, and 25 nm for textured silicon bottom cells) was sputtered from a NiO_x target using 100 W power with pure Ar at 1 mTorr on the silicon bottom cell with ITO layer. All other charge transport extraction layers, namely p-doped TaTm-CS90112, intrinsic TaTm and C_{60} were deposited using the same protocol as for the single junction devices. However, to account for the increased surface area of the textured devices (nano- and micro-textured) the deposited thickness was increased by a factor of 1.7. This adjustment was not applied in the case of the planar tandem solar cell. For the tandem devices BCP is replaced

by ALD-deposited SnO_2 which serves as buffer layer to protect the underlaying stack from the harsher TCO deposition. SnO_2 is deposited via ALD using an Arradiance's GEMStar XT Thermal ALD system integrated into an N_2-filled glovebox. For SnO_2 deposition, the ALD chamber is heated to 60 °C, the bottle containing the Sn precursor tetrakis(dimethylamino)tin (TDAT) was heated to 60°C, and the bottle of water (oxidizer) was not heated. The precursor manifolds were heated to 115 and 140 °C respectively. The SnO_2 deposition process consists of a series of purges of TDAT for 550 ms and water vapor for 200 ms, each of them followed by N_2 purges to clear off the precursors from the ALD chamber. For the front contact, a 45 nm IZO layer was used as a transparent electrode, deposited via sputtering. The active area of 1.04 cm^2 was defined by the subsequently vacuum-deposited Ag electrode (350 nm and 600 nm for planar and textured configurations respectively, with three additional 100 µm-thick grid-fingers).

Solar Cell Characterization

Current-Voltage Analysis (*J-V*)

Single-Junction Perovskite Solar Cells

J-V curves were recorded using a Keithley 2612A sourcemeter in a -0.2 and 1.2 V voltage range, with 0.01 V steps and integrating the signal for 20 ms after a 10 ms delay, corresponding to a scan speed of about 0.1 Vs^{-1}. The devices were illuminated under a Wavelabs Sinus 70 LED solar simulator. The light intensity was adjusted before every measurement using a calibrated Si reference diode. The active area, defined as the overlap between the bottom ITO and the top metal electrodes, was 5.5 × 1.5 mm^2. For the characterization under illumination, a shadow mask defining an area of 5 × 1 mm^2 was used.

Two-Terminal Perovskite/Silicon Tandem Solar Cells

The *J-V* characteristics of the perovskite/silicon TSCs were measured with a class AAA LED-based solar simulator (Wavelabs, LS-2) with a scan rate set at 0.6 Vs^{-1} using a sourcemeter (Keithley 2400) with an air-mass 1.5 global (AM1.5G) spectra (100 $mWcm^{-2}$). The solar simulator irradiation intensity was calibrated using a certified silicon solar cell (Fraunhofer ISE). The measurement was performed in ambient atmosphere. A shadow mask defining an area of 1 × 1 cm^2 was used was the measurements.

External Quantum Efficiency (EQE)

Single-Junction Perovskite Solar Cells

For the sensitive EQE measurements, the cell was illuminated by a QuartzTungsten-Halogen lamp (Newport Apex 2-QTH) through a monochromator (Newport CS130-USB-3-MC), a chopper at 279 Hz and a focusing lens. The device current was measure as a function of energy from 2.1 eV to 1.2 eV in 0.02 eV steps using a lock-in amplifier. The system was calibrated, and the solar spectrum mismatch was corrected using a calibrated silicon reference cell. Fast EQE measurements were performed on a QE-R system from Enlitech.

Two-Terminal Perovskite/Silicon Tandem Solar Cells

EQE was measured using an Enlitech QE-R Quantum Efficiency System. To measure the spectral response of each sub-cell in the 300 to 1200 nm range we use a beam spot with an area of 1 mm^2. A halogen lamp is used to illuminate the sub-cell for which the EQE is not being analyzed. When the EQE of the perovskite top cell was analyzed an 850 nm long pass filter was applied to the halogen lamp to saturate the current generated by the SHJ bottom cell, and

when the EQE of the SHJ bottom cell was analyzed a 550 nm short pass filter was used to saturate the current generated by the perovskite top cell. The current mismatch generated within the tandem device by this light bias leads to a shift in the operating voltage of the sub-cell being measured. Hence, without a voltage bias the sub-cell under measurement is in reverse bias and therefore a bias voltage is needed to bring it back to short-circuit conditions. The voltage bias applied is in the range of the V_{OC} of the non-analyzed sub-cell, that is around 0.6 V when analyzing the EQE of the perovskite top cell and around 1.0 V when analyzing the EQE of the SHJ bottom cell.

Suns-V_{OC} with selective Illumination

Suns-V_{OC} with selective illumination enables the estimation of the open-circuit voltage (V_{OC}) generated by each subcell in a tandem device. The measurement is performed by illuminating each subcell independently and measuring the resulting V_{OC}. Specifically, a blue LED with a peak wavelength of 450 nm is used to excite the perovskite sub-cell, while a 940 nm diode selectively illuminates the silicon sub-cell.

X-ray diffraction (XRD)

XRD patterns were collected in Bragg–Brentano geometry on an Empyrean PANalytical powder diffractometer with a copper anode operated at 45 kV and 40 mA.

Scanning Electron Microscopy (SEM)

Scanning Electron Microscopy (SEM) was performed with a high-resolution field-emission Hitachi SU8010 microscope operating at an accelerating voltage of 2 kV over platinum-metallized samples. Steady state photocarrier grating (SSPG) measurements were carried out using a He–Ne laser with 15 mW power and 632 nm wavelength.

Grazing-Incidence Wide-Angle X-ray Scattering (GIWAXS)

The GIWAXS images were acquired with a Bruker D8 Advance machine. Primary track: unpolarized Cu K-alpha X-ray source (40 kV, 40 mA), Goebel mirror, 0.5 mm micromask, 0.3 mm snout; secondary track: DECTRIS Eiger2 R 500 2D detector; sample-to-detector distance: 118.1 mm. A grazing-incidence angle of 1.7° and an exposure time of 1 h were employed for measurement. GIWAXS images processing and analysis were performed utilizing the GIXSGUI MATLAB toolboxes.[35]

k-Imaging (Intensity-dependent Photoluminescence-mapping)

Two 467 nm LED bars powered excite the sample in an 45° symmetrical alignment. The image is recorded by a sCMOS camera equipped with a macro zoom lens and an exposure time of 500 ms. To eliminate the detection of excitation light and other noise, a 695 nm absorptive long-pass filter is attached to the lens and a background correction performed. Images are recorded intensity dependent within an excitation range, equivalent to 0.005-0.2 suns based on photon flux. The k-factor is extracted as the exponent from fitting the intensity dependent PL intensities pixel-wise with a power law model and aggregated as a heat map.[32]

Acknowledgements

Funded by the European Union; views and opinions expressed are however those of the authors only and do not necessarily reflect those of the European Union or CINEA; neither the European Union nor the granting authority can be held responsible for them. NEXUS project has received funding from Horizon Europe Research and Innovation Action program under Grant Agreement nº 101075330. The cooperation and research exchange was funded by the Karlsruhe House of Young Scientists (KHYS).The authors gratefully acknowledge financial support by the Helmholtz Association (project Zeitenwende, Solar Technology Acceleration Platform (Solar TAP), program-oriented funding period IV of the Helmholtz Association (Materials and Technologies for the Energy Transition, Topic 1: Photovoltaics and Wind Energy, Code: 38.01.02)), the Helmholtz Energy Materials Foundry, the German Federal Ministry for Economic Affairs and Climate Action (BMWK) through the project SHAPE (03EE1123A), and the Karlsruhe School of Optics and Photonics (KSOP). This research was carried out as part of the HyPer project, which is funded by the CETPartnership, under the Joint Call 2023. The CETPartnership' s research projects are co-funded by the European Commission (Grant Agreement No. 101069750) and the national funding organizations listed on the CETPartnership website. The BMWE funding for the KIT is also listed under the funding code 03EE1222B. Authors acknowledge also support from the Comunitat Valenciana (MFA/2022/022 and CISEJI/2022/43) as well as from the Ministry of Science and Innovation (MCIN), and the Spanish State Research Agency (AEI): PCI2024-155048-2 project funded by MICIU/AEI/10.13039/501100011033 and co-funded by the European Union; grant RYC2019-027187-I funded by MCIN/AEI/10.13039/501100011033 and by "ESF Investing in Your Future; PID2021-126444OB-100 funded by MICIU/AEI/10.13039/501100011033" and "ERDF A way of making Europe".

Contributions

A.D. and **S.C.-B.** equally contributed to the conceptualization, methodology, investigation, visualization, figure preparation and original draft preparation. **L.G.-E.**, **F.V.**, **I.G.-F.**, **C.R.-C.**, **T.Z.** and **J.P.** assisted in investigation, device fabrication and device characterization. **P.C.** and **D.M.** fabricated the silicon bottom cells. **L.G.-E.**, **M.S.** and **P.F.** assisted with supervision. **U.W.P.** and **H.J.B.** equally conceptualized and supervision the project. They were leading equally the project administration, reviewing and editing of the manuscript.

References

1. Abzieher, T. *et al.* Vapor phase deposition of perovskite photovoltaics: short track to commercialization? *Energy Environ Sci* **17**, 1645–1663 (2024).

2. Kosasih, F. U., Erdenebileg, E., Mathews, N., Mhaisalkar, S. G. & Bruno, A. Thermal evaporation and hybrid deposition of perovskite solar cells and mini-modules. *Joule* **6**, 2692–2734 (2022).

3. Vaynzof, Y. The Future of Perovskite Photovoltaics—Thermal Evaporation or Solution Processing? *Adv Energy Mater* **10**, 2003073 (2020).

4. Petry, J. *et al.* Industrialization of Perovskite Solar Cell Fabrication: Strategies to Achieve High-Throughput Vapor Deposition Processes. *EES Solar* **1**, 404–418 (2025).

5. Aydin, E. *et al.* Pathways toward commercial perovskite/silicon tandem photovoltaics. *Science* vol. 383 1–13 Preprint at https://doi.org/10.1126/science.adh3849 (2024).

6. Yang, C. *et al.* Achievements, challenges, and future prospects for industrialization of perovskite solar cells. *Light: Science and Applications* vol. 13 13:227 Preprint at https://doi.org/10.1038/s41377-024-01461-x (2024).

7. Jacobsson, T. J. *et al.* An open-access database and analysis tool for perovskite solar cells based on the FAIR data principles. *Nat Energy* **7**, 107–115 (2021).

8. Abzieher, T. *et al.* Continuous flash sublimation of inorganic halide perovskites: overcoming rate and continuity limitations of vapor deposition. *J Mater Chem A Mater* **12**, 8405–8419 (2024).

9. National Renewable Energy Laboratory (NREL), Best Research-Cell Efficiencies. https://www.nrel.gov/pv/cell-efficiency.html (2025).

10. Ritzer, D. B. *et al.* Upscaling of perovskite solar modules: The synergy of fully evaporated layer fabrication and all-laser-scribed interconnections. *Progress in Photovoltaics: Research and Applications* **30**, 360–373 (2022).

11. Paliwal, A., Zanoni, K. P. S., Roldán-Carmona, C., Hernández-Fenollosa, M. A. & Bolink, H. J. Fully vacuum-deposited perovskite solar cells in substrate configuration. *Matter* **6**, 3499–3508 (2023).

12. Ávila, J., Momblona, C., Boix, P. P., Sessolo, M. & Bolink, H. J. Vapor-Deposited Perovskites: The Route to High-Performance Solar Cell Production? *Joule* **1**, 431–442 (2017).

13. Feng, J. *et al.* High-throughput large-area vacuum deposition for high-performance formamidine-based perovskite solar cells. *Energy Environ Sci* **14**, 3035–3043 (2021).

14. Gil-Escrig, L. *et al.* Fully Vacuum-Processed Perovskite Solar Cells on Pyramidal Microtextures. *Solar RRL* **5**, (2021).

15. Roß, M. *et al.* Co-Evaporated Formamidinium Lead Iodide Based Perovskites with 1000 h Constant Stability for Fully Textured Monolithic Perovskite/Silicon Tandem Solar Cells. *Adv Energy Mater* **11**, 2101460 (2021).

16. Leyden, M. R. *et al.* Loading Precursors into Self-Assembling Contacts for Improved Performance and Process Control in Evaporated Perovskite Solar Cells. *Solar RRL* **8**, 2400575 (2024).

17. Zhou, J. *et al.* Highly efficient and stable perovskite solar cells via a multifunctional hole transporting material. *Joule* **8**, 1691–1706 (2024).

18. Piot, M. *et al.* Fast Coevaporation of 1 µm Thick Perovskite Solar Cells. *ACS Energy Lett* **8**, 4711–4713 (2023).

19. Dewi, H. A., Erdenebileg, E., De Luca, D., Mhaisalkar, S. G. & Bruno, A. Accelerated $MAPbI_3$ Co-evaporation: Productivity Gains without Compromising Performance. *ACS Energy Lett* **9**, 4319–4322 (2024).

20. Ihrenberger, J. *et al.* Solution-Free Growth of CsPbBr3 Perovskite Films Using a Fast and Scalable Close Space Sublimation Method. *Cryst Growth Des* **24**, 5542–5548 (2024).

21. Rodkey, N. *et al.* Close-Space Sublimation as a Scalable Method for Perovskite Solar Cells. *ACS Energy Lett* **9**, 927–933 (2024).

22. Li, G., Ho, J. Y. L., Wong, M. & Kwok, H. S. Low cost, high throughput and centimeter-scale fabrication of efficient hybrid perovskite solar cells by closed space vapor transport. *Physica Status Solidi - Rapid Research Letters* **10**, 153–157 (2016).

23. Guesnay, Q. *et al.* Pizza Oven Processing of Organohalide Perovskites (POPOP): A Simple, Versatile and Efficient Vapor Deposition Method. *Adv Energy Mater* **14**, (2024).

24. Duan, C. *et al.* Stoichiometric Gradient Rebalancing Achieves Surface Reconstruction and Bulk Homogenization in High-Performance Vapor-deposited Perovskite Solar Cells†. *J Mater Chem A Mater* **13**, 24675–24684 (2025).

25. Dou, Y. *et al.* Enhanced Buried Interface Engineering for Efficient Inverted Perovskite Solar Cells Fabricated via Vapor–Solid Reaction. *Small Methods* **9**, (2025).

26. Duan, C. *et al.* Oriented Growth for Efficient and Scalable Perovskite Solar Cells by Vapor–Solid Reaction. *Adv Funct Mater* **34**, 2313435 (2024).

27. Wang, Y. *et al.* Grain Boundary Elimination via Recrystallization-Assisted Vapor Deposition for Efficient and Stable Perovskite Solar Cells and Modules. *Advanced Materials* **35**, (2023).

28. Luo, L. *et al.* 19.59% Efficiency from Rb0.04-Cs0.14FA0.86Pb(BryI1−y)3 perovskite solar cells made by vapor–solid reaction technique. *Sci Bull (Beijing)* **66**, 962–964 (2021).

29. Gil-Escrig, L. *et al.* Efficient and Thermally Stable Wide Bandgap Perovskite Solar Cells by Dual-Source Vacuum Deposition. *Adv Funct Mater* **33**, 2214357 (2023).

30. Chozas-Barrientos, S. *et al.* Molecular Recombination Junction for Vacuum-Deposited Perovskite/Silicon Two-Terminal Tandem Solar Cells. *ACS Energy Lett* **10**, 1733–1740 (2025).

31. Hacene, B. *et al.* Imaging of Recombination Rates and Lifetime in Perovskite Thin Film Processing. *Small Methods* **9**, 2402119 (2025).

32. Petermann, J. *et al.* Advanced Photoluminescence Imaging Method for Robust and Scalable Perovskite Quality Monitoring in Monolithic Tandem Solar Cells. *Solar RRL* **9**, 2500074 (2025).

33. Er-raji, O. *et al.* Toward efficient and industrially compatible fully textured perovskite silicon tandem solar cells: Controlled process parameters for reliable perovskite formation. *Progress in Photovoltaics: Research and Applications* **33**, 86–99 (2025).

34. Pappenberger, R. *et al.* Versatile Two-Step Process for Perovskite-Based Tandem Photovoltaics. *Solar RRL* **9**, 2500193 (2025).

35. Jiang, Z. *GIXSGUI*: a MATLAB toolbox for grazing-incidence X-ray scattering data visualization and reduction, and indexing of buried three-dimensional periodic nanostructured films. *J Appl Crystallogr* **48**, 917–926 (2015).